Weekly to annual variability of surface soil moisture

Xuan Xi[1], Pierre Gentine[1]

[1] Department of Earth and Environmental Engineering, Columbia University, New York, NY, USA

Corresponding author: Pierre Gentine (pg2328@columbia.edu)

Key Points:

- 17 climate models in CMIP5 are used to evaluate the temporal behavior of surface soil moisture compared to the observations.
- Models underestimate frequencies smaller than the seasonal time scale and overestimate frequencies larger than it.
- At a global scale, model biases are more closely related to climate than to soil types.

Abstract

Soil moisture is important for sub-seasonal and seasonal climate prediction. However, biases and uncertainties of soil moisture in climate models affect the accuracy of climate prediction. Here we evaluate biases in climate model soil moisture across different time scales in the frequency domain. Based on our findings, compared to observations, soil moisture variability in the models is found to be underestimated at frequencies smaller than the seasonal time scale and overestimated at frequencies larger than the seasonal time scale. In addition, for the total effect of evapotranspiration and precipitation variability on soil moisture, models also underestimate frequencies smaller than the seasonal time scale and overestimate frequencies larger than it. Furthermore, no matter which factor (evapotranspiration or precipitation) is most affecting soil moisture, models underestimate its effect on soil moisture in the corresponding frequency range. Finally, at a global scale, biases in climate models can be related to the mean climate and not to soil properties. This study provides new insights into climate models deficiencies, and contributes to a better understanding of soil moisture and climate.

Plain Language Summary

Soil moisture is important for climate prediction at subseasonal to seasonal time scales. It is closely related to processes between the atmosphere and the land surface, such as evapotranspiration and precipitation. However, the deficiencies in climate models on soil moisture lead to incorrect predictions. In this study, we found that (1) models underestimate soil moisture variability on weekly to seasonal time scales and overestimate it on seasonal to annual time scales, (2) soil moisture has a closer relationship with precipitation on weekly to seasonal time scales and has a closer relationship with evapotranspiration on seasonal to annual time scales, but models underestimate these relationships on weekly to annual time scales, and (3) the deficiencies in these climate models are more closely related to mean soil moisture than soil properties (i.e., sand & clay content). Our study provides a new understanding and assessment of climate models based on soil moisture variability.

1 Introduction

Even though soil moisture only constitutes a small part of the total water on the Earth, it has been regarded as one of the most important factors in the Earth system. Because of its special role at the boundary between the land surface and atmosphere, soil moisture plays an important role in land-atmosphere interactions and climate-change projections (Koster et al., 2004; Seneviratne et al., 2010). It is critical for the hydrologic cycle as soil moisture impacts the ecosystem (D'Odorico et al., 2003), agriculture (Botter et al., 2007), and the terrestrial carbon cycle (Green et al., 2019).

It is therefore important to understand the variability of soil moisture and its relationship to atmospheric processes over different time scales. Most previous studies used the autocorrelation of the soil moisture time series to investigate this topic. First, soil moisture variability was modeled as a first-order Markov process forced by a random precipitation series (i.e., white noise) and an exponential damping term related to evapotranspiration losses (Delworth and Manabe, 1988). Based on this model, the authors first proposed that a red noise process can reasonably govern the temporal variability of soil moisture, and the e-folding autocorrelation time scale of a red noise process can be used to quantify soil moisture variability (Delworth and Manabe, 1988). However, since there are some important limitations in this Markovian framework (Koster and Suarez, 2001), following studies tried to improve the understanding of

soil moisture variability. To solve the problem about the possibility of seasonal variations as well as the possible ignored persistence in forcing, a more complete framework and a revised version (Seneviratne and Koster, 2012) based on a comprehensive soil moisture autocorrelation equation was proposed to further analyze soil moisture memory (Koster and Suarez, 2001). The integral time scale based on autocorrelation function was also used as another memory metric in the study of soil moisture variability (Ghannam et al., 2016; Katul et al., 2007). In addition, the temporal spectrum of soil moisture was analyzed to evaluate evapotranspiration and precipitation variability on soil moisture spectra on various time scales (Katul et al., 2007; Nakai et al., 2014). These methods are based on models where soil moisture treated as a red noise process. To solve the deficiencies of this model when applying it to models and observations with finer resolutions, a new study replaced the e-folding time scale of the red noise model with two new parameters, thus dividing soil moisture memory into short-term and long-term components (McColl et al., 2019).

Even though soil moisture variability has received increasing interests in recent years, applications on short-term and seasonal prediction are still relatively open (Seneviratne et al., 2010). Satellite remote sensing (Berg and Sheffield, 2018) now provide global observations of soil moisture, including the Soil Moisture Ocean Salinity (SMOS) mission (Kerr et al., 2010), and the Soil Moisture Active Passive (SMAP) mission (Entekhabi et al., 2010). These can be used to better explain land-atmosphere interactions over different spatiotemporal scales (Guillod et al., 2015; Tuttle and Salvucci, 2016) and its feedbacks (McColl et al., 2019). Indeed, since the physical processes involved into land-atmosphere interface are complex (Berg and Sheffield, 2018), climate models still exhibit too many biases in soil moisture memory across different time scales (Katul et al., 2007; Koster and Suarez, 2001; Nakai et al., 2014; Seneviratne et al., 2006; Seneviratne and Koster, 2012).

Based on this, this study performs a comparative analysis between climate models from CMIP5 and soil moisture observations to highlight deficiencies in modeled soil moisture across time scales. The soil moisture used in this study is surface soil moisture (SSM). Although root zone soil moisture (RZSM) has stronger control on hydrological fluxes such as evapotranspiration, several studies have demonstrated that SSM is well correlated with RZSM (Akbar et al., 2018; Ford et al., 2014). In this way, SSM can be regarded as a proxy for RZSM under most conditions, especially on weekly to annual time scales (McColl et al., 2019). This study highlights model deficiencies using: 1) SSM variability; 2) the effect of evapotranspiration (ET) and precipitation (P) variability on SSM in the frequency domain. Results are divided into three frequency ranges, which represent 1) weekly to monthly time scales, 2) monthly to seasonal time scales, and 3) seasonal to annual time scales, to show the deficiencies in the models over different time scales.

2 Data

2.1 Model data

The fifth phase of the Climate Model Intercomparison Project (CMIP5), as in earlier CMIP phases, was proposed to integrate a set of experiments that offer state-of-the-art multimodel perspective to improve our knowledge on climate change and climate variability (Taylor et al., 2012). In this study, the daily output of 17 CMIP5 models from the historical simulation is used. To characterize SSM variability as well as the effect of ET and P variability on SSM (i.e., atmospheric water loss and supply), we analyze the output of SSM (top 10cm; variable *mrsos* in

the CMIP5 archive), ET (*hfls*), and P (*pr*). We use only one ensemble member – "r1i1p1" (where *r* for realization, *i* for initialization, and *p* for physics,) – when more than one member is available. The models are selected based on the availability of daily output data required for the spectral analysis. Table S1 in the supplemental material lists all models used in this study as well as their corresponding centers, forcings, spatial resolution, and temporal coverage.

2.2 Observation data

Observation data needs to be compared with model data to determine the biases in climate models. In this study, SMAP (Entekhabi et al., 2010), GLEAM (Miralles et al., 2011a; Miralles et al., 2011b), and ERA5 (Copernicus Climate Change Service (C3S), 2017) are used as the observation dataset for SSM, ET, and P, respectively. To make sure that the data is consistent, we use datasets with the same temporal coverage, spanning 1 April 2015 to 31 March 2018. In the final part of this study, we also analyze the relationship between model biases and global soil properties using Global Soil Dataset for use in Earth System Models (GSDE) (Shangguan et al., 2014) as the corresponding dataset.

2.2.1 SMAP soil moisture data

The Level 3 products from the NASA Soil Moisture Active Passive (SMAP) mission is used as the reference observation of SSM in this study. The NASA SMAP satellite was launched in January 2015 and measured SSM (i.e., moisture in the top ~5 cm of the soil column) globally every 2~3 days (Entekhabi et al., 2010). Originally, SMAP included an active L-band radar and a passive L-band radiometer planning to provide soil moisture observations at 3 km and 36 km spatial resolution, respectively, to get 9 km soil moisture product based on both of them. However, due to an instrument anomaly, the radar stopped working in July 2015. On the other hand, the radiometer continues to provide observation for SSM. We use three years of 6:00 a.m. descending half-orbit passes, version 5 L3 SMAP passive soil moisture retrievals (O'Neill et al., 2018). The reason to use morning observations rather than evening observations is that the air, vegetation, and near-surface soil are assumed to be in thermal equilibrium in the early morning hours for the radiometer soil moisture algorithm; thus, there is less degradation in the retrievals than at 6:00 p.m. ascending half-orbit passes. Here, the level 3 product is made using geophysical parameters derived from Level 1 and 2 products, and be spatiotemporally re-sampled to the global cylindrical EASE-Grid 2.0 (Brodzik et al., 2012). In this projection, regardless of longitude and latitude, each grid cell has a nominal size of approximately 36×36 km^2, and the dimensions of all global data arrays are 406 rows and 964 columns.
Comparison between SMAP and in situ SSM observations demonstrate that SMAP is meeting its performance target considering the difference between the lateral and vertical support of the satellite and in situ soil moisture observations (Chan et al., 2016; Shellito et al., 2016; Colliander et al., 2017). In addition, when comparing to other soil moisture satellites, SMAP had the highest accuracy (Chen et al., 2018).

2.2.2 GLEAM evapotranspiration data

The Global Land Evaporation Amsterdam Model (GLEAM) is a set of algorithms that separately estimate all components of ET (Miralles et al., 2011a; Miralles et al., 2011b). GLEAM is a global model primarily driven by satellite-based remotely sensed observations. The core of the GLEAM model uses the modified Priestley-Taylor equation (Priestley and Taylor, 1972), which calculates

daily potential E_p based on observations of surface air temperature and surface net radiation. This method quantifies ET based on remotely sensed observation. Although being sensitive to uncertainties in its forcing and ancillary data (Hsu et al., 2017), and not error-free compared to in situ observations (Yang et al., 2017), GLEAM has been commonly used in studies of the global hydrological cycle (Greve et al., 2014; Jasechko et al., 2013; Zhang et al., 2016). A detailed description of GLEAM can be obtained in previous studies (Miralles et al., 2011a; Miralles et al., 2011b; Martens et al., 2016, 2017).
In this study, we use three years of GLEAM 3.3a, which is a global dataset spanning the 39-year period 1980–2018, derived based on reanalysis radiation and air temperature, a combination of gauge-based, reanalysis, and satellite-based precipitation, as well as satellite-based vegetation optical depth (Miralles et al., 2011a; Martens et al., 2017). The dataset is provided on a 0.25 °×0.25 ° latitude-longitude grid with a temporal resolution of one day.

2.2.3 ERA5 precipitation data

ERA5 is the fifth generation reanalysis of ECMWF (European Centre for Medium-Range Weather Forecasts). This reanalysis is achieved by data assimilation, which combines weather forecasts with observations in an optimal way every few hours to produce the best estimate of the state of the atmosphere. In this way, ERA5 is a combination of model data and observations into a globally complete and consistent dataset.
In this study, we use three years of hourly "total precipitation" estimates of variables on single levels as the observation of precipitation (Copernicus Climate Change Service (C3S), 2017). This dataset has a spatial resolution of 0.25 °×0.25 ° for the atmosphere, spanning the period from 1979 to present with hourly temporal resolution.

2.2.4 GSDE soil data

The Global Soil Dataset for use in Earth System Models (GSDE) is a dataset that provides soil information including 11 types of general soil information for soil profiles and 34 soil properties for eight depths (Shangguan et al., 2014). In this study, we only use two main soil properties – sand and clay contents, to find their relationships with biases in the models.
The data in the GSDE dataset has two different resolutions, i.e., 30 seconds (~1km) and 5 minutes (~10km). In this study, we use the second one. In addition, all soil properties are separated into eight layers with different depths. Since we mainly focus on surface soil moisture, here only the first two layers (0-0.045 and 0.045-0.091m) of sand and clay contents are used, and we take the average of them for further analysis.

3 Materials and Methods

3.1 Data preprocessing and preparation

In this study, both observation and model data need to be preprocessed. For SMAP data, small gaps because of instrument maneuvers, data downlink anomalies, and data quality screening, can cause poor data quality as well as missing data. Therefore, SMAP values that do not range in the valid range from 0.02 to 0.5 are removed. In addition, since SMAP does not perform global observations every day, and because of missing data, the SSM for each pixel is temporally discontinuous. Therefore, the missing values are filled to solve this data discontinuity. Firstly, we used a moving median with a window of length 10 to fill the missing data. We tried different window sizes up to 80 but found no major differences. For the filled results, we replaced values

less than 0.02 by 0.02, and larger than 0.5 by 0.5, to make sure that all SSM data were in a valid range.

For model data, since the time series of soil moisture span decades or even centuries, there might be trends for some regions. We remove these trends using linear regression from the data to focus the analysis on the sub-annual and annual fluctuations of the soil moisture itself. Here, for SSM of all models, we subtract an optimal (least squares) fitted linear regression so that the trended data has a mean value of zero.

3.2 Normalized variability of SSM, ET and P

Normalized variability of SSM (SSM_n), ET (ET_n), and P (P_n) for both models and observations are used for comparative analysis between them. Here, we explain our strategy with SSM_n as an example; the processes for ET_n and P_n are similar.

The method to get SSM_n for models and observation are the same. It is based on the fast Fourier transform (FFT), which is a faster algorithm of the discrete Fourier transform (DFT).

First, we use FFT to get the spectrum of SSM. Since all datasets used are at a temporal resolution of one day, the corresponding sampling frequency (f_s) is one day^{-1}, and the sampling numbers (N) is the number of days for each dataset. In the frequency domain, the length of the spectrum is $N/2 + 1$ and the largest frequency is $F_s/2$. In addition, since the spectrum is symmetric, only half of it is used, as $(0: N/2) * f_s/N$.

Then we get the energy spectrum of SSM based on its amplitude spectrum as $E_{SSM}(\omega) = |F_{SSM}(\omega)|^2$. In this study, we restrict our analysis to weekly to yearly time scale. Since gap filling and instrumental noise of SMAP data (section 3.1) may introduce day-to-day variability as noise in the observation, while this noise usually does not exist in model data since models are smoother than observations, we remove the power spectrum below seven days (i.e. frequency above 1/7) to make model data and observation data more comparable by smoothing the observation data. For $E_{SSM}(\omega)$ with $1/N$ ~ 1/365 day^{-1}, unlike modeling data with multi-decade records, the temporal coverage of the observation data in this study is only three years. This temporal coverage is too small to make reasonable analysis on inter-annual time scales and thus we omit the lowest frequencies.

Next, we separate $E_{SSM}(\omega)$ into three frequency ranges: 1/30 ~ 1/7, 1/90 ~ 1/30, 1/365 ~ 1/90 day^{-1}. They represent the temporal variability of SSM at weekly to monthly time scales, monthly to seasonal time scales, and seasonal to annual time scales, respectively. Dividing the spectral energy of $E_{SSM}(\omega)$ in each frequency range by the total spectral energy of $E_{SSM}(\omega)$ for all three frequency ranges, the ratio of the spectral energy for each frequency range is:

$$SSM_{n_i} = \frac{\sum_j \left|SSM_i(\omega_j)\right|^2}{\sum_{i=1}^{3} \sum_j \left|SSM_i(\omega_j)\right|^2} \quad (1)$$

where $SSM_i(\omega_j)$ is the amplitude value of SSM spectrum for *j*th frequency in *i*th frequency range, and SSM_{n_i} is the normalized variability of SSM in *i*th frequency range with a range from zero to one. According to the Parseval theorem, the spectral energy of SSM in the time domain and the frequency domain are equivalent. ET_n and P_n for both models and observations are also obtained based on the same method.

3.3 Effect of ET and P on SSM variability

Both ET and P control the SSM variability, ET decreases SSM while P increases it. Here we

want to find the effects of ET and P variability on SSM spectra over different time scales.
In the time domain, based on an assumed linear time-invariant system, the relationship between SSM and ET time series data as well as SSM and P time series data can be characterized by the relative impact of ET and P, respectively on the SSM variability as:

$$ssm_{et}(t) = et(t) \otimes h_{se}(t) = \int_{-\infty}^{+\infty} ET(t-\tau) * h_{se}(\tau) d\tau \quad (2)$$

$$ssm_{p}(t) = p(t) \otimes h_{sp}(t) = \int_{-\infty}^{+\infty} P(t-\tau) * h_{sp}(\tau) d\tau \quad (3)$$

where $ssm(t)$, $et(t)$, and $p(t)$ are the time series of SSM, ET, and P, and $h_{se}(t)$ and $h_{sp}(t)$ are transfer functions between SSM and ET as well as SSM and P. It is hard to capture these transfer functions in the time domain. However, the convolution theorem can be applied to these two processes to convert convolution operations in the time domain into multiplication in the frequency domain as:

$$SSM(\omega) = ET(\omega) \cdot H_{SE}(\omega) \quad (4)$$

$$SSM(\omega) = P(\omega) \cdot H_{SP}(\omega) \quad (5)$$

where $SSM(\omega)$, $ET(\omega)$, and $P(\omega)$ are the amplitude spectrum of $ssm(t)$, $et(t)$, and $p(t)$, and $H_{SE}(\omega)$ and $H_{SP}(\omega)$ are the Fourier transforms of $h_{se}(t)$ and $h_{sp}(t)$. In terms of the energy spectrum, this reads as:

$$|SSM(\omega)|^2 = |ET(\omega)|^2 \cdot |H_{SE}(\omega)|^2 \quad (6)$$

$$|SSM(\omega)|^2 = |P(\omega)|^2 \cdot |H_{SP}(\omega)|^2 \quad (7)$$

Based on the two equations, the effects of ET and P variability on SSM spectra are related to $|H_{SE}(\omega)|^2$ and $|H_{SP}(\omega)|^2$, respectively. To capture these effects over different time scales, two ratios are calculated by:

$$H_{SE_{n_i}} = \frac{SSM_{n_i}}{ET_{n_i}} \quad (8)$$

$$H_{SP_{n_i}} = \frac{SSM_{n_i}}{P_{n_i}} \quad (9)$$

where $H_{SE_{n_i}}$ and $H_{SP_{n_i}}$ is the fraction of SSM_n to ET_n and P_n in the ith frequency range, respectively. However, it can be hard to define the dominant factor on SSM variability only based on these two ratios. So we first calculate the fraction of SSM variability to the sum of ET and P variability (i.e., demand and supply) and then calculate the fraction of ET variability to the sum of ET and P variability as:

$$H_{SEP_{n_i}} = \frac{SSM_{n_i}}{ET_{n_i} + P_{n_i}} = \frac{1}{\frac{1}{H_{SE_{n_i}}} + \frac{1}{H_{SP_{n_i}}}} \quad (10)$$

$$H_{EEP_{n_i}} = \frac{ET_{n_i}}{ET_{n_i} + P_{n_i}} \quad (11)$$

where $H_{SEP_{n_i}}$ represents the total effect of ET and P variability on SSM, and $H_{EEP_{n_i}}$ represents the proportion of ET variability to all effects on SSM by ET and P variability (i.e., the fraction of ET variability compared to that of precipitation). Thus, based on these two ratios, it is easier to determine the dominant factor on SSM dynamics in each frequency range.

3.4 Spectral slope of SSM, ET, and P

The spectral slope exhibits characteristics of the soil moisture physical behavior. This factor can show how the variability of ET and P contribute to the spectrum of soil moisture (Katul et al., 2007). First, all spectra are normalized by the variance of their respective temporal range to avoid the spectra from high variance regions overwhelm the spectra from low variance regions (Delworth and Manabe, 1988). Then, within each frequency range, we fit a linear regression for the slope of the energy of all frequencies based on the least-squares approach. In this way, each spatial point has three spectral slopes in the different frequency ranges, so they can be more easily compared.

When considering SSM, ET, and P as power-law noise signals, the color of noise, which is referred to their energy spectrum, can be used to identify spectral slopes of the three variables. The analysis of colored noise has been studied for a long time. It was brought to attention by Steele, who suggested the color of terrestrial and marine noise should be different (Steele, 1985). A further study (David, 2004) performed an analysis of the variance spectra of long-term time series of environmental variables and made a specific conclusion on these colored noises. The color of the noise can be divided into several main types according to the slope of the power spectral density. In this study, we use six kinds of colored noise (violet, blue, white, pink, red, and black) to characterize the spectral slopes for SSM ($SSM_{k\omega}$), ET ($ET_{k\omega}$), and P ($P_{k\omega}$). The corresponding spectral slope of violet, blue, white, pink, and red noise (or Brownian noise) is 2, 1, 0 (the spectral density of white noise is flat), -1, and -2, respectively, and the spectral slope of black noise is smaller than -2. The smaller the slope of the spectrum in the frequency domain, the longer the memory of the time series signals for white, pink, red, and black noise.

3.5 Bias between models and observations

There are three kinds of biases between the models and observations that we are evaluating here: 1) Biases in SSM_{n_i}; 2) Biases in $H_{SEP_{n_i}}$ and $H_{EEP_{n_i}}$; and 3) Biases in $SSM_{k\omega}$, $ET_{k\omega}$, and $P_{k\omega}$. All three biases are calculated as the difference between models minus observation. In addition, the coefficient of variation across models is calculated to show the uncertainties across models.

The spatial resolutions between models and observations, as well as between models and observations themselves, are all different. Therefore, the dataset for each model and the observations are re-gridded to the same spatial resolution. Here we use the spatial resolution of SMAP (36 km×36 km) as the reference and project all other datasets to this "standard" spatial resolution using a minimized distance:

$$\mathrm{D}(m, m') = \arg min \left|\left(m'_p - m_p\right) + \left(m'_q - m_q\right)\right| \tag{12}$$

where $\mathrm{D}(m, m')$ is the shortest distance between the non-SMAP pixel and the SMAP pixel, m and m' are SMAP pixel and non-SMAP pixel, p and q are latitude and longitude to the corresponding pixel, respectively. In this way, all data have the same spatial resolution and then can be used to get the mean and the coefficient of variation of the results across all models.

In addition, a significance test is performed on the averaged biases maps among models and depicted in the maps using stippling. The reason for that is some biases shown in averaged maps may only due to several models or even one model. These biases with less significance should not be considered. The significance here is defined as the ratio of the number of models with the same sign as average biases in each pixel to the number of total models. On the final map, stippling shows the regions that passed the significance test of 100% (17/17 model) and 80% (14/17 model), respectively.

4 Results

This section shows the global map of SSM_n, ET_n, and P_n, as well as the effect of ET_n and P_n on SSM_n over different time scales based on the observations. In addition, results of models are compared with observations to find the deficiencies of models, and to find the relationship between models biases with the mean SSM and two soil properties.

4.1 Observations

Figure 1 shows the global distribution of SSM_n, ET_n, and P_n over different time scales. For SSM, the spectral energy concentrates more on the seasonal to annual time scale for most regions, while have the smallest proportion in the weekly to monthly time scales. This means that SSM variability is most important at seasonal time scales.

For ET, the largest ET_n in the lowest frequency range means that ET variability is important at seasonal time scales. The spectral energy of ET concentrates at long time scales for most regions except in regions with a tropical wet climate. The reason is that ET has a large seasonal cycle in many regions driven by radiation or moisture limitation except in wet tropics where radiation and moisture variability is small. In this way, results in tropical wet regions, such as Amazon Rainforest, Africa's Near Equator, Indonesia, and the Philippines, are the opposite. In these regions, most spectral energy concentrates on time scales shorter than monthly. This smaller variability in radiation variability is mainly due to that the variability of cloud weekly time scale (or longer) will cause a large variability of ET in short time scales (Anber et al., 2015). Moreover, this mechanism has the largest influence on regions near the equator because these regions receive more radiations than other regions all the time. Therefore, in these regions, ET variability is mostly located in the high-frequency range. In addition, ET in desert regions does not have a clear seasonal cycle as well due to the limitation of moisture.

For P, P_n shows different regional distribution over different time scales: it is larger on seasonal to annual time scales for most tropical regions where the seasonal cycle can be large, while larger on weekly to monthly time scales for other regions, especially in non-tropical regions. The reason is that, in tropical regions, especially regions with tropical wet and dry climate, although the changes in the temperature and the radiation across seasons are small, rainfall exhibits a strong seasonal cycle. So P in these regions shows strong seasonal variability. However, in tropical regions with a tropical very wet climate, such as the Democratic Republic of the Congo, Indonesia, and the Philippines, there is no such an apparent seasonal cycle because of the regular rainfall and constant temperatures in these regions. On the other hand, there is not an obvious rainy and dry season distinction for non-tropical regions. The occurrence of rainfall is typically more random over the whole year and close to a white noise signal at high frequencies (Katul et al., 2007; Nakai et al., 2014) (Figure 1). Therefore, P variability in non-tropical regions is almost all in the high-frequency variability, except in monsoonal regions of central America, Sahel, etc.

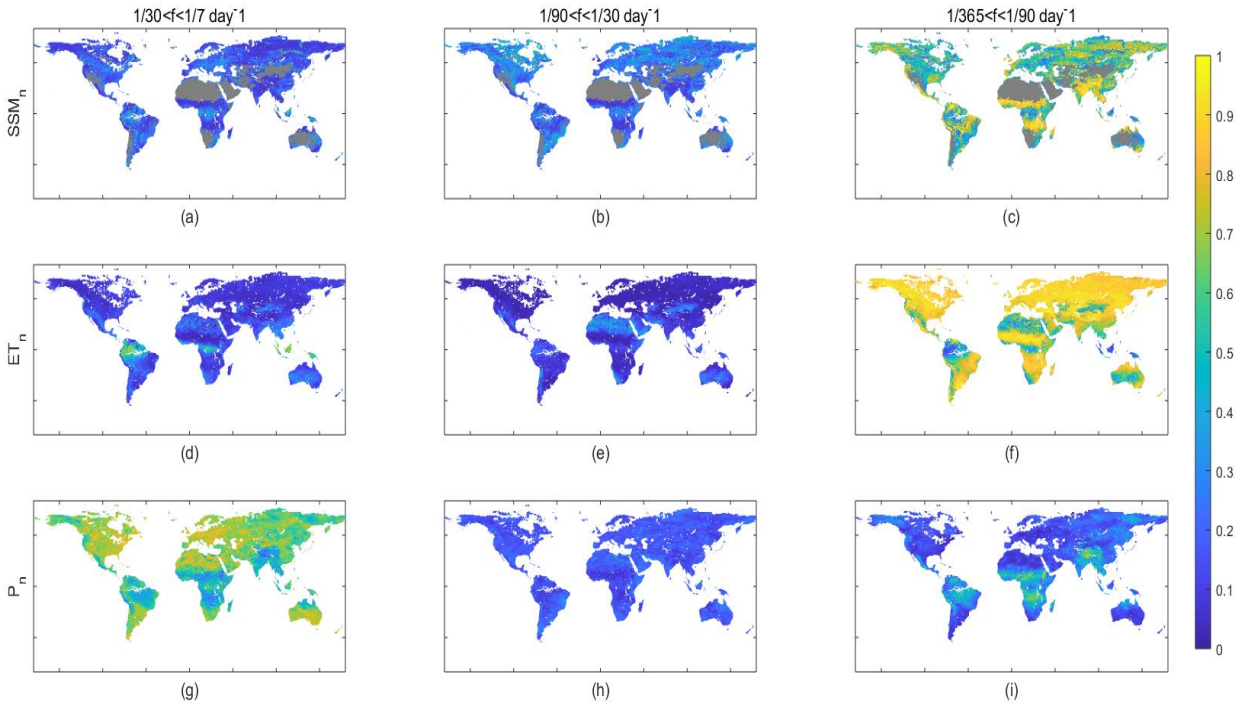

Figure 1. SSM_n (Figure a-c), ET_n (Figure d-f), and P_n (Figure g-i) over different time scales. The three columns from left to right represent results at weekly to monthly time scales, monthly to seasonal time scales, and seasonal to annual time scales. SSM_n, ET_n, and P_n represent the fraction of variability (also referred to as energy) in each frequency range to total variability for SSM, ET, and P, respectively. Grey parts in Figure a-c are regions with SSM less than 0.1. For ET_n, and P_n, results of regions not shown in SSM_n are removed (e.g., Antarctica), that is, maps of the three variables have totally the same spatial resolution and field vision.

Although an apparent regional distribution can be found for both ET_n and P_n, the SSM_n distribution is more diverse. Figure 2 shows the global distribution of H_{SEP_n} and H_{EEP_n} over different time scales. For shorter time scales (weekly to monthly), ET and P variability has little effect on SSM. Compare to P variability, the fluctuation of ET nearly has limited effects on SSM as ET is a slower process in part regulated by SM. For longer time scales, the effect of ET and P on SSM increases. At monthly to seasonal time scales where the total effect of ET and P on SSM reaches its largest magnitude, even though the proportion of ET variability becomes larger, P is still the dominant factor of SSM variability. For longer time scales (seasonal to annual), the total variability of ET and P decrease, but is still larger than it in the largest frequency range. However, in this frequency range, ET becomes the dominant factor. Therefore, P variability alone is no longer able to explain the SSM dynamics. Since H_{EEP_n} represents the proportion of ET variability to the total variability of ET and P, similar to the results of ET_n shown in Figure 1, results of H_{EEP_n} are opposite in tropical wet regions, where ET variability has more effect on SSM on shorter time scales (weekly to seasonal), and P becomes the dominant factor on longer time scales (seasonal to annual) due to seasonality in rainfall regimes.

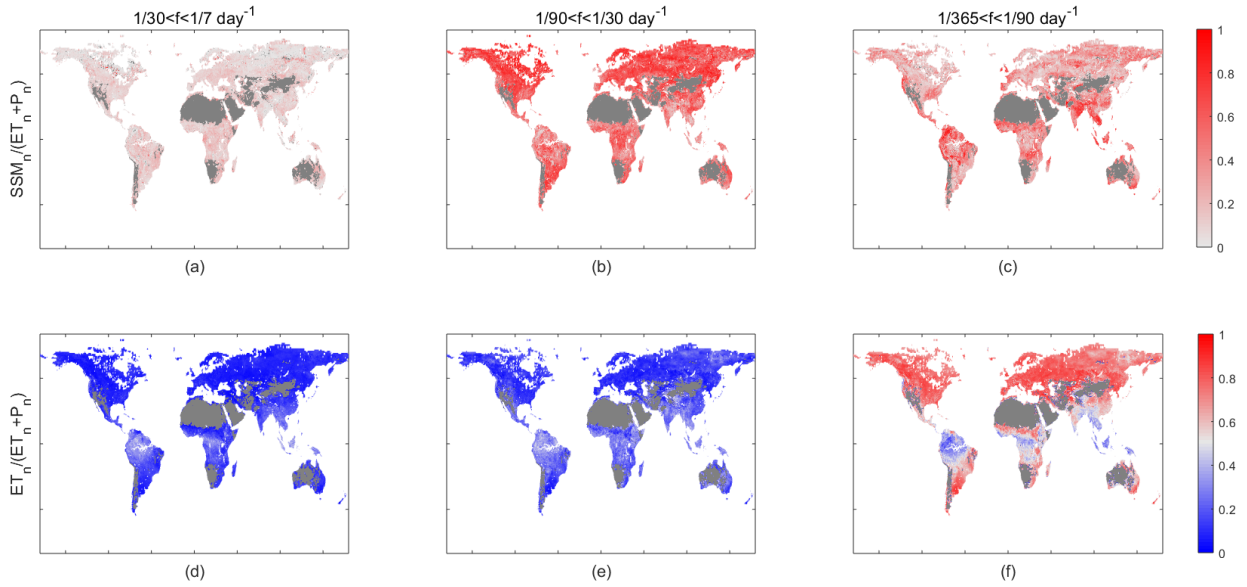

Figure 2. H_{SEP_n} (Figure a-c) and H_{EEP_n} (Figure d-f) over different time scales. H_{SEP_n} is the ratio of SSM_n to the sum of ET_n and P_n, which represents the total effect of ET and P variability on SSM; H_{EEP_n} is the ratio of ET_n to the sum of ET_n and P_n, which represents the proportion of ET variability to all effects on SSM by ET and P. Grey parts are regions with SSM less than 0.1. The three columns from left to right represent results at weekly to monthly time scales, monthly to seasonal time scales, and seasonal to annual time scales. Values in each frequency range are normalized across the whole frequency range to have a span from zero to one.

To further describe the ET and P effect on SSM variability, we first evaluate relationships between SSM spectra and ET spectra as well as P spectra. Figure 3 shows the global distribution of the spectral slopes of SSM, ET, P, and E_p over different time scales expressed in terms of noise color. Within each frequency range, the smaller the spectral slope, the more spectral energy concentrates on longer time scales.

There is a phase shift between SSM and P spectra in the two larger frequency ranges, especially on times above the monthly time scale. At weekly to monthly time scales, regions with the smaller spectral slope of P lead to SSM spectra decay more rapidly. In most regions where P is a white noise, SSM is a red noise in the corresponding regions, indicating longer memory induced by soil moisture (Salvucci and Entekhabi, 1994). On the other hand, in regions where P is a pink noise, like Central America, eastern and southern Africa, southern Asia, eastern and southern Brazil, and northern Australia, SSM is a black noise. A similar phase shift between SSM and P spectra can also be found for some regions at monthly to seasonal time scales, such as southern North America, southern and north-central Asia, and regions around the Mediterranean, but those are not as evident as for the largest frequency range since the effect of ET variability on SSM increases little in this frequency range. On seasonal to annual time scales, the dominant factor on SSM variability is ET rather than P, and there is no strong relationship between the P and SSM spectra. In addition, there is no phase shift between the ET and SSM spectra, even in the seasonal to annual time scales, where ET is the dominant factor on SSM variability.

In previous studies, ET was shown to be related to the damping term of the SM spectra (Delworth and Manabe, 1988; Katul et al., 2007; Nakai et al., 2014) which modulates potential evaporation. The differences between the spectra of ET and E_p are mainly due to the variability of soil moisture. E_p is an estimate of the maximum evaporation rate according to different meteorological conditions (Delworth and Manabe, 1988). Therefore it is relatively random on

shorter time scales reflecting weather fluctuations as white or pink noise. However, ET, unlike E_p, is closely related to soil moisture as it limits the supply of moisture to the atmosphere on longer time scales. So the SSM dynamics influence the ET spectrum – leading to a more red noise because SSM has a longer memory than E_p. This influence is especially more visible in dry regions. The reason is that, compared to SSM in dry regions, SSM in wet regions is mostly saturated and thus mostly track the variability of potential evaporation. So ET in wet regions will not be strongly affected by SSM variability. For longer time scales, both ET and E_p show an obvious seasonal cycle that dominates the signal.

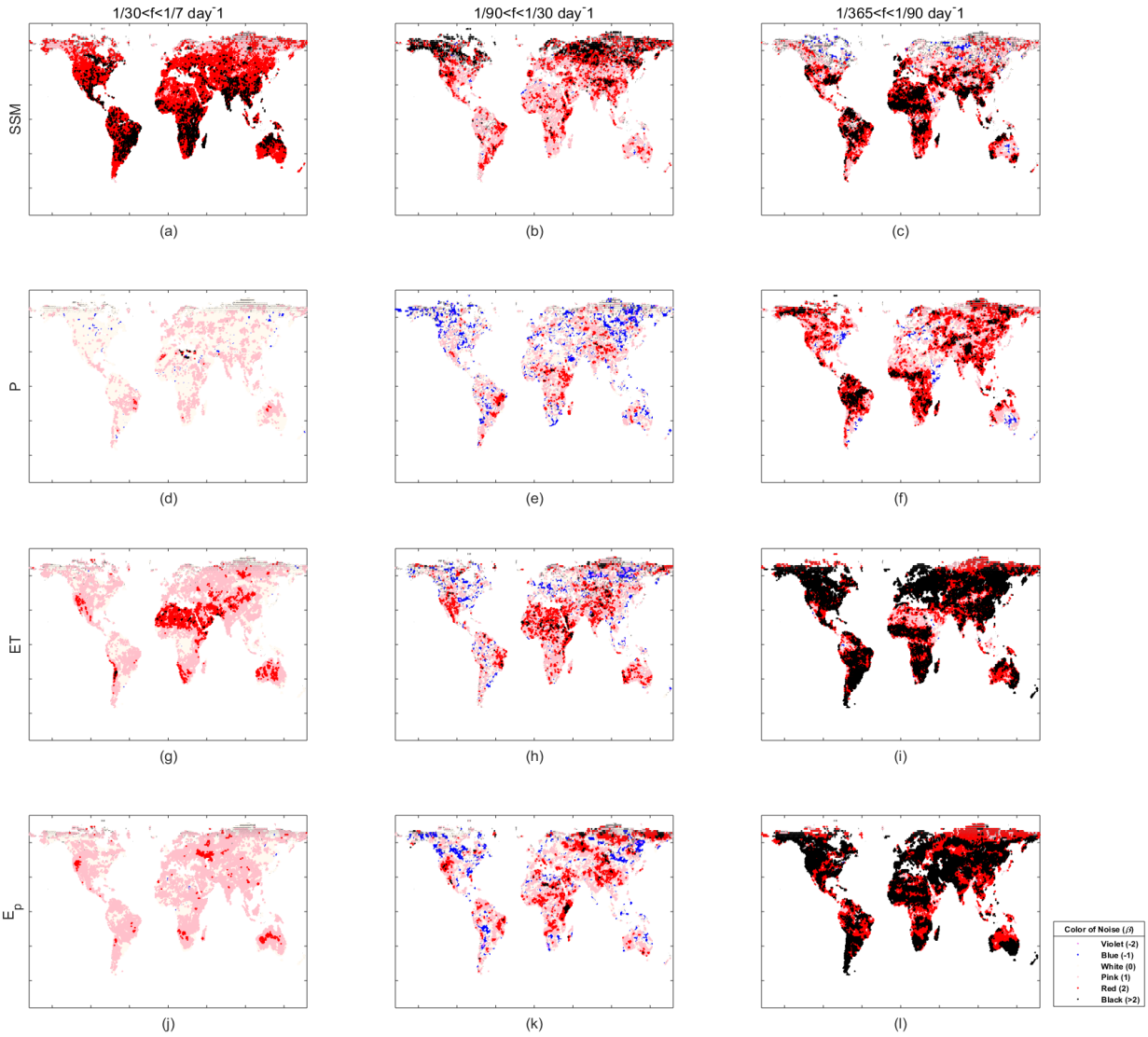

Figure 3. Noise color of SSM (Figure a-c), ET (Figure d-f), P (Figure g-i), and potential evaporation (Figure j-l) over different time scales. The colors in each figure represent the corresponding color of noise refers to the energy spectrum of SSM, ET, and P. Considering SSM, ET, and P as examples of power-law noise, their spectral densities vary as inverse frequency, more precisely are proportional to $1/f^{\beta}$ (Bourke, 1998). In the legend, the number in parentheses followed by each color refers to the corresponding β, which is also the inverse number of the spectral slope. The spectral slope of violet noise, blue noise, white noise, pink noise, and red noise (or Brownian noise) is 2, 1, 0 (the spectral density of white noise is flat), -1, and -2, respectively, and

the spectral slope of black noise is smaller than -2. The three columns from left to right represent results at weekly to monthly time scales, monthly to seasonal time scales, and seasonal to annual time scales.

4.2 Comparison between models and observations

Figure 4a-c show the averaged biases for SSM_n of models compared to the observation. A significance test is performed on these three maps and depicted using stippling. Here, the + stippling means the region passes a 100% significance test (i.e., all 17 models have the same sign of biases as the averaged value), and the dot stippling means the region passes an 80% significance test (i.e., 14 of the 17 models have the same sign as the averaged value). Therefore, we only focus on the regions with stippling. Based on these results, for most regions, the model biases are negative for the two higher frequency ranges, while they are positive for the lowest frequency range. Models underestimate SSM variability on weekly to seasonal time scales, while they overestimate it on seasonal to annual time scales. The largest biases appear in Eastern Europe, Central and Eastern North America, Central Asia, and regions near the equator. However, in a few other regions like India and southern Brazil, where the model biases are positive for the two higher frequency ranges while are negative for the lowest frequency range, the results are contrary to most regions. Since the mean of SSM_n in each frequency range is different, the coefficient of variation is used here to see the degree of variation across all models (Figure 4d-f). These results show that the coefficient of variation is smaller at lower frequencies for most regions. Therefore, climate models have larger SSM uncertainties at shorter time scales (weekly to monthly) and smaller uncertainties at longer time scales (seasonal to annual).

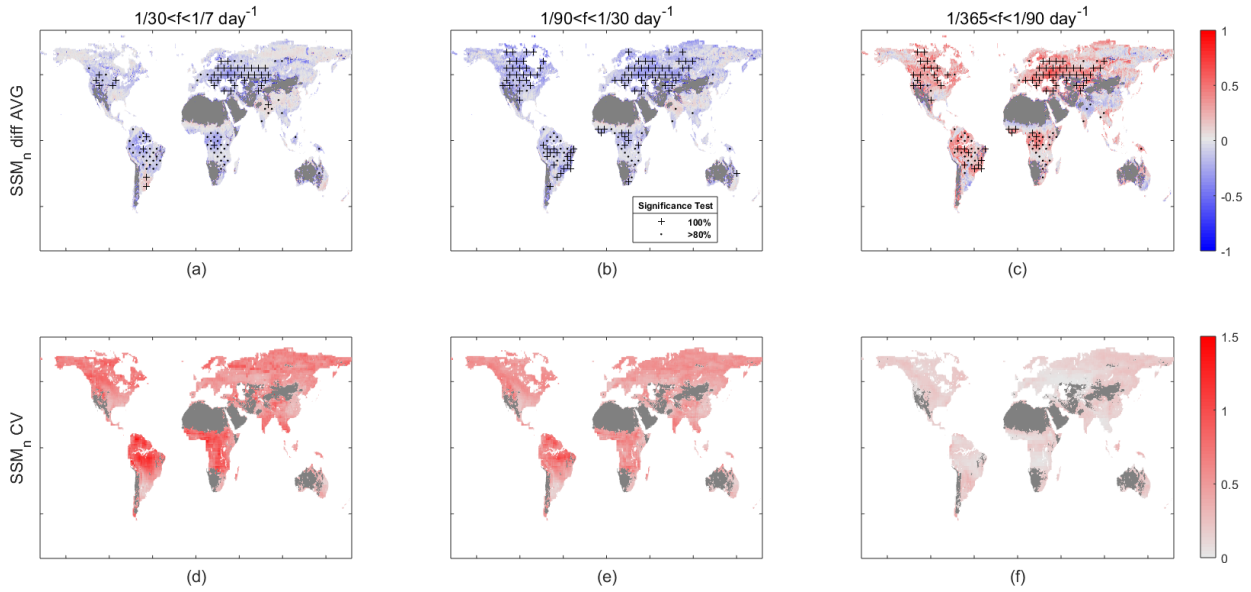

Figure 4. Model deficiencies of SSM_n over different time scales. Figure (a-c) are averaged biases for SSM_n of models compared to the observation, and figure (d-f) are the coefficient of variation of SSM_n across all models. SSM_n represents the intermodel spread in each frequency range to total variability for SSM. For Figure a-c, averaged biases of SSM_n are calculated by model data minus observation data. For Figure d-f, the coefficient of variation of SSM_n is calculated by the standard deviation of SSM_n divided by the mean of SSM_n for each frequency range. Grey parts are regions with SSM less than 0.1. The three columns from left to right represent results at weekly to monthly time scales, monthly to seasonal time scales, and seasonal to annual time scales. For averaged biases of SSM_n (Figure a-c), plus stippling means the region passes a 100% significance test, and dot stippling means the region passes an 80% significance test.

Based on the result shown in Figure 4, the biases and uncertainties in climate models are further analyzed with the mean SSM on a global scale. Figure S1 shows the global distribution of the normalized mean SSM based on SMAP data. From Figure 5a-c, for all three frequency ranges, the biases mainly concentrate in regions with larger mean SSM content (about 45% ~ 85%). Biases at weekly to annual time scales of SSM in these climate models mainly concentrate in wetter regions. This result is consistent with the result shown in Figure 6. From a latitude averaged perspective, larger biases of SSM_n are seen in regions near the equator and mid-latitude regions in the northern and southern hemispheres, which have higher mean SSM values. On the other hand, models nearly have no SSM_n biases in mid-latitude regions around 30º N and 30º S, where the mean SSM has lower values (Figure 6d). For uncertainties in these climate models, Figure 5d-c show that the coefficient of variation for SSM variability decreases as the frequency decreases. In addition, for all three frequency ranges, the coefficient of variation is higher in regions with intermediate mean SSM (about 40% ~ 60%) and smaller mean SSM (about 5% ~ 15%), showing a different characteristic compared to the biases in the models. To sum up, when considering SSM intermodal spread, the frequency range with larger biases has smaller intermodal uncertainties and vice versa. Besides, climate models show the least deficiencies in regions with mean SSM from 15% to 40%, typical of semi-arid regions, such as central Argentina, southern Sahara Desert, regions near Tropic of Capricorn in Africa, southern India, and northern and eastern coasts of Australia.

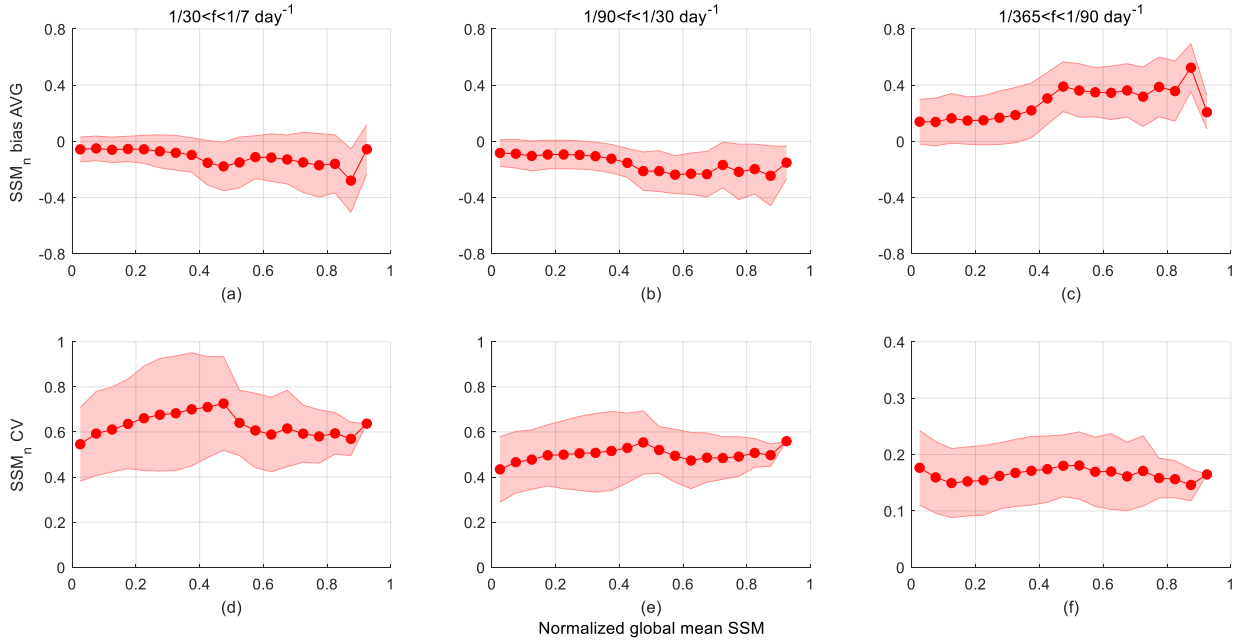

Figure 5. SSM_n for models and the observation as a function of mean SSM for observation over different time scales. Figure 5a-c are averaged biases of SSM_n between models and observations, and figure 5d-f are coefficient of variation of SSM_n across all models. The three columns from left to right represent results at weekly to monthly time scales, monthly to seasonal time scales, and seasonal to annual time scales. SSM is separated into 20 bins of equal size (i.e., 0.05 for each bin), and the averaged biases and coefficient of variation of SSM_n located in each bin (i.e., range of global mean SSM) were calculated, respectively.

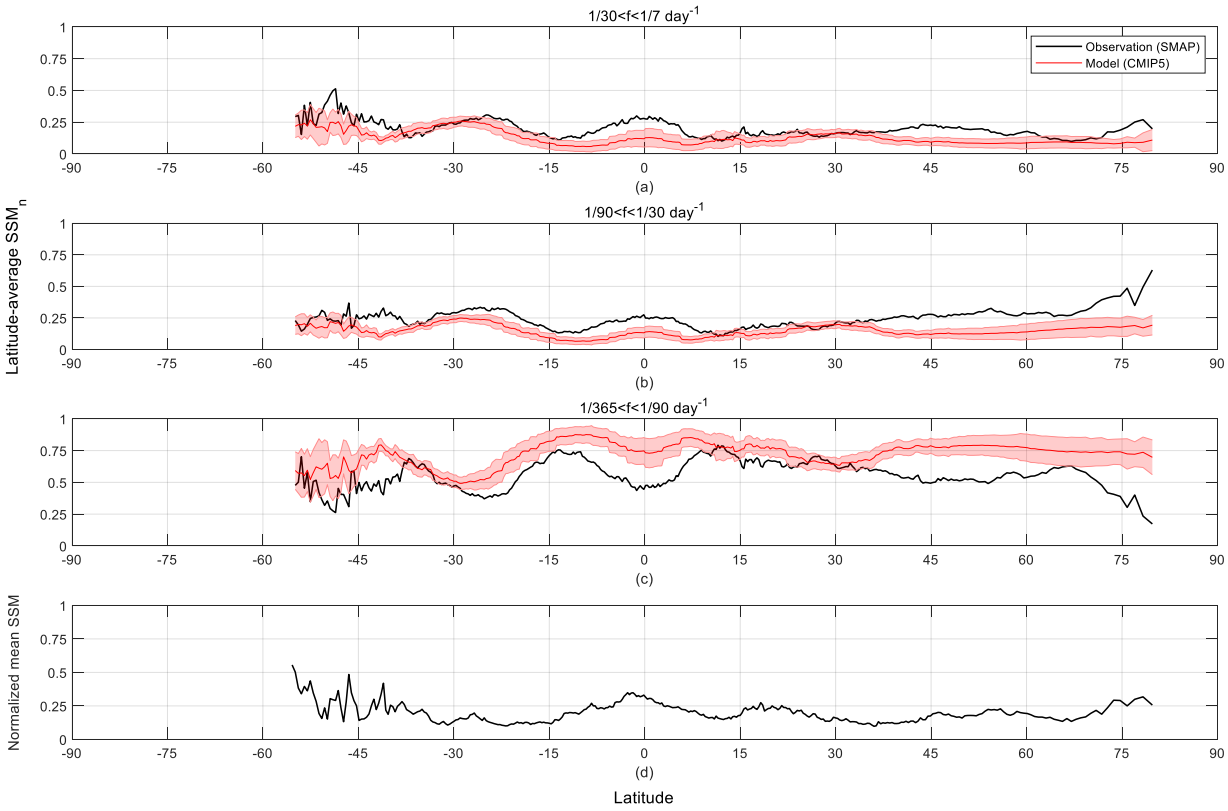

Figure 6. Latitudinal average of SSM_n for models and SMAP observations over different time scales. Black lines are results of observation, and red lines are results of the models. The first three rows from top to bottom (i.e. Figure a-c) represent results at weekly to monthly time scales, monthly to seasonal time scales, and seasonal to annual time scales, respectively. The average of SSM_n for each latitude is calculated as the y value. Regions with SM less than 0.1 are removed. In addition, Figure d shows the mean of renormalized global mean SSM (in Figure 1) for each latitude.

Similar to the averaged biases of SSM_n (Figure 4a-c), for most regions, the models underestimate the total effect of ET and P variability on SSM at weekly to seasonal time scales while they overestimate it at seasonal to annual time scales (Figure 7a-c). In addition, the largest biases of models are on monthly to seasonal time scale range, and for each frequency range, in regions with larger biases similar to SSM_n. We already know that P variability dominates SSM dynamics at weekly to seasonal time scales while ET dominates it at seasonal to annual time scales (Figure 2d-f), no matter which factor is dominant, models tend to underestimate its effect on SSM. For example, on weekly to monthly time scales where P is the dominant factor, models overestimate the proportion of ET variability to the total variability of ET and P. Thus, the P effect on SSM is underestimated by models. In addition, models show larger biases on H_{SEP_n} than H_{EEP_n} (Figure 7), which means that models do relatively well at capturing the proportion of ET and P variability to their total variability, while they exhibit larger biases on the total effect of ET and P on SSM variability.

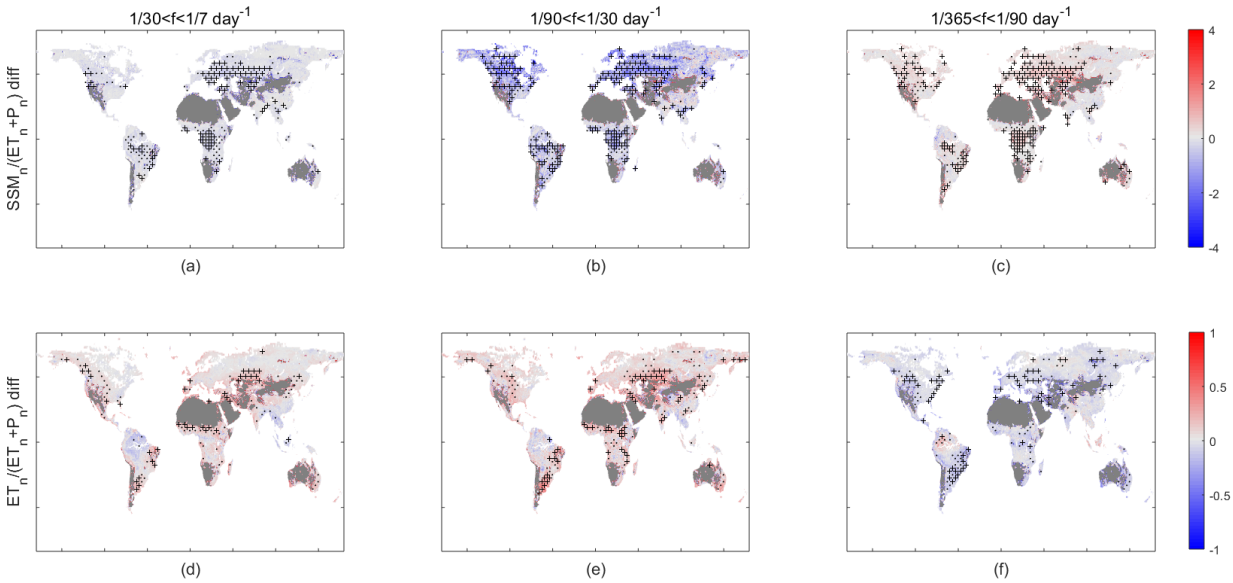

Figure 7. Averaged biases of H_{SEP_n} (Figure a-c) and H_{EEP_n} (Figure d-f) between models and the observation over different time scales. For each figure, averaged biases are calculated by model data minus observation data. Grey parts are regions with SSM less than 0.1. The three columns from left to right represent results at weekly to monthly time scales, monthly to seasonal time scales, and seasonal to annual time scales. For each figure, plus stippling means the region passes a 100% significance test, and dot stippling means the region passes an 80% significance test.

Then, biases in H_{SEP_n} and H_{EEP_n} as a function of the global mean SSM are analyzed to see if there is any relationships between them (Figure 8). For H_{SEP_n}, biases of models are mainly concentrated in regions with larger mean SSM (about 45% ~ 85%) across the frequency range. On the other hand, for H_{EEP_n}, models achieve their best performance in transition zones (regions where SSM approximate equals 0.4), while as mean SSM either increases or decreases, biases of models increase. Therefore, when considering ET and P intermodal spread effect on SSM, biases of models tend to be more apparent in wetter and drier regions where the SSM variability is dominated by strong seasonality. In addition, when further investigating the proportion of ET and P variability, drier regions (with SSM about 5% ~ 15%) also need to be considered for biases of the dominant factors.

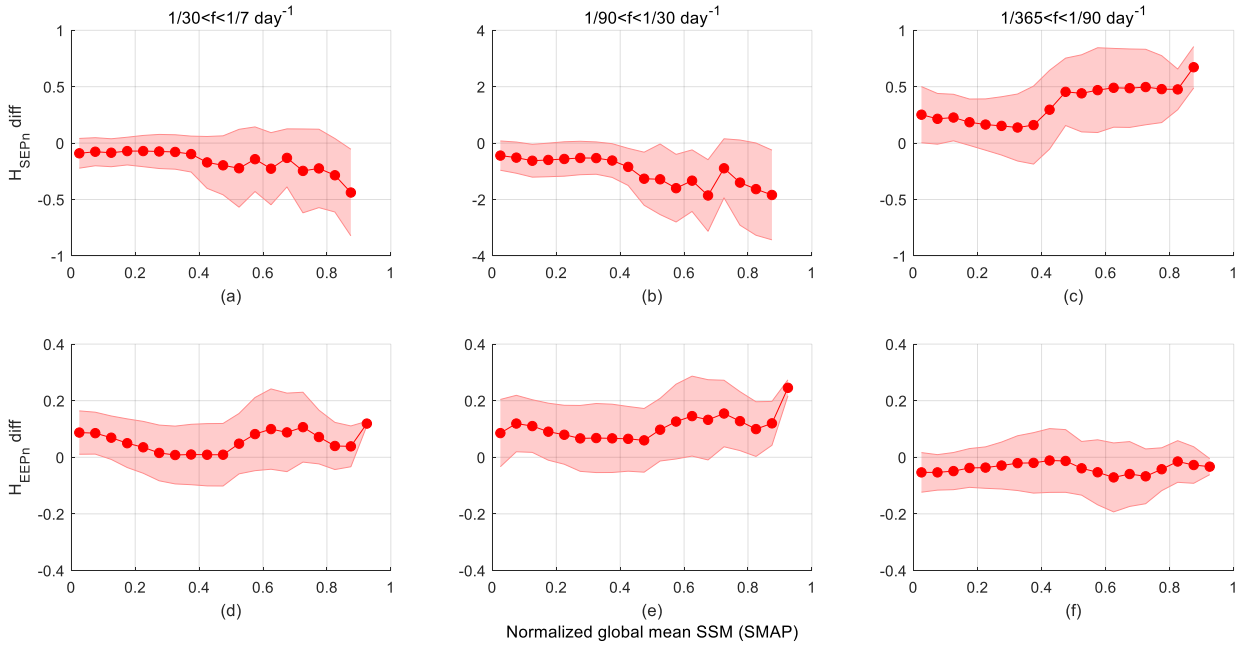

Figure 8. Averaged biases of H_{SEP_n} (Figure a - c) and H_{EEP_n} (Figure d - f) between models and the observation with global mean SSM for observation in different time scales. The three columns from left to right represent results at weekly to monthly time scales, monthly to seasonal time scales, and seasonal to annual time scales, respectively. The method to make this figure is similar to Figure 5.

In addition to the averaged biases of models compared to observations, the coefficients of variation of H_{SEP_n} and H_{EEP_n} across models are also investigated to understand the spread across models (Figure S2). For both H_{SEP_n} and H_{EEP_n}, the intermodel spread is larger on shorter time scales (weekly to seasonal) than those on longer time scales (seasonal to annual), which means models have greater variance at weekly to seasonal time scales. Based on Figure 7 and Figure S2, it can be concluded that, for ET and P variability effect on SSM, models have larger spread at shorter time scales, where they underestimate the variability. On the other hand, at longer time scales, the overestimated biases are mostly similar across models, pointed towards a systematic deficiency of land surface models to represent long-term variability.

So far, the biases in models were found to be tightly related to mean SSM content. Apart from that, it is also important to see whether these biases relate to the soil itself. Here, two of the main soil properties are used – sand and clay content – to evaluate this dependence. Figure S3 shows the global distribution of these two properties for the first two layers in the GSDE dataset. Here the mean for these two layers is used to see its relationship with model biases. No matter whether it is the biases of SSM variability or the effect of ET and P variability on SSM, the two soil properties do not impact the relationships (Figure S4 and S5). This means that it is not the soil itself that lead to biases of climate models found in this study, but this point rather to issues in the representation of other processes regulating soil moisture such as vegetation, which regulate the transpiration and long-term soil moisture response (Kennedy et al., 2019). For instance, plant water stress based on plant hydraulics has shown superior results when compared to typical water-stress responses (Kennedy et al., 2019), especially on seasonal time scales.

Finally, biases of the spectral slopes $SSM_{k\omega}$, $ET_{k\omega}$, and $P_{k\omega}$ (Figure 9) shows that models have shorter memory than observations. Positive biases mean that models underestimate the memory in each frequency range and vice versa. For SSM, ET, and P, models underestimate their memory

for most regions with high significance, and this underestimation is largest in the lowest frequency range (seasonal to annual). This can again relate to difficulties in the representation of long-term transpiration and the dynamics of soil moisture.

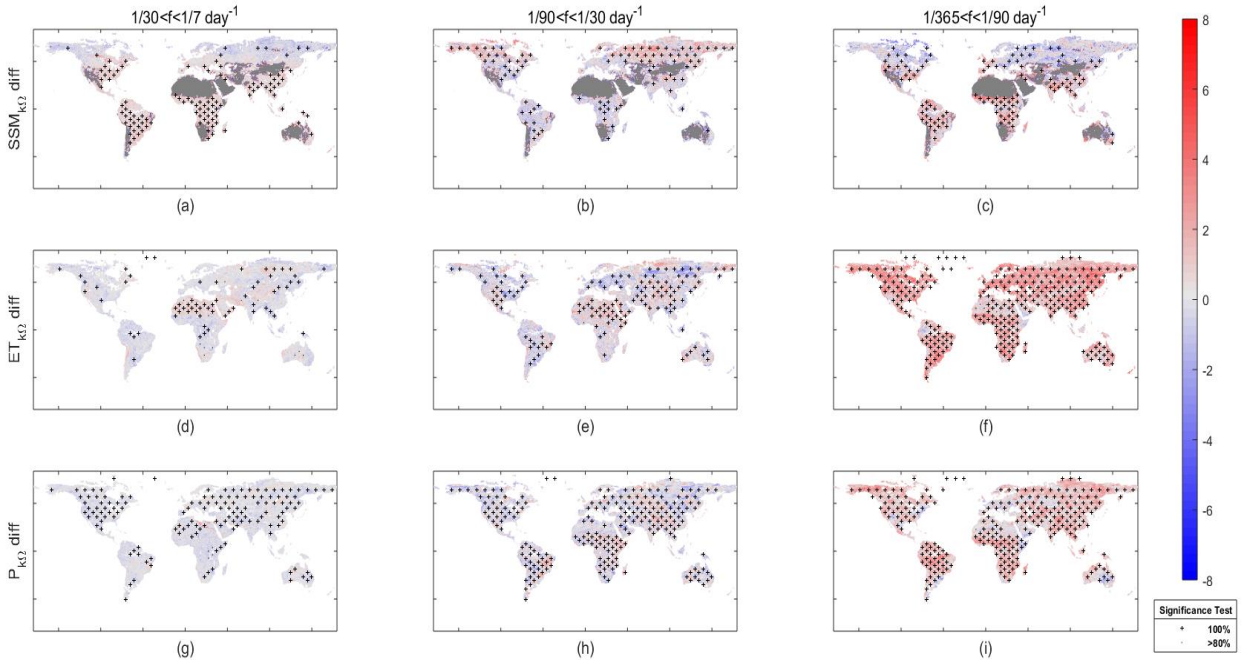

Figure 9. Averaged biases of spectral slope biases for $SSM_{k\omega}$ (Figure a-c), $ET_{k\omega}$ (Figure d-f), and $P_{k\omega}$ (Figure g-i) between models and the observation over different time scales. Grey parts in Figure a-c are regions with SSM less than 0.1. The three columns from left to right represent results at weekly to monthly time scales, monthly to seasonal time scales, and seasonal to annual time scales. For each figure, plus stippling means the region passes a 100% significance test, and dot stippling means the region passes an 80% significance test.

5 Conclusions

This research presents a comparative analysis between CMIP5 climate models and satellite observations of surface soil moisture variability at a global scale. It also investigates the effects of evapotranspiration and precipitation variability on soil moisture spectra over different time scales. Biases in models are found by comparing the results of models and observations, and uncertainties in models are found by comparing results across all models. By performing statistical analysis on model biases with the global distribution of mean SSM and soil properties, the relationships highlight some causes of the model deficiencies.

Models underestimate SSM variability at the higher frequency range (weekly to seasonal) while they overestimate it in the lower frequency range (seasonal to annual). These biases concentrate in wetter regions ($0.45 <$ normalized $\overline{SSM} < 0.85$). Models exhibit larger uncertainties at longer time scales (monthly to annual). In addition, the frequency range with larger biases in models will show smaller uncertainties. For each frequency range, intermodal spread in the bias is larger in regions of intermediate wetness.

For ET and P variability effects on SSM (H_{SEP_n} and H_{EEP_n}), models underestimate the total effect of ET and P variability on SSM in the higher frequency range (weekly to seasonal) while they overestimate it in the lower frequency range (seasonal to annual). Furthermore, whether ET or P is the dominant factor of variability, models underestimate their effect on SSM variability.

For H_{SEP_n}, biases are more concentrated in wetter regions (normalized $\overline{SSM}$ > 0.45); for H_{EEP_n}, biases are more concentrated in wetter regions (normalized $\overline{SSM}$ > 0.45) and drier regions (normalized $\overline{SSM}$ < 0.15). In addition, similar to SSM_n, models exhibit larger uncertainties as the frequency increases. For biases of SSM_n, H_{SEP_n} and H_{EEP_n}, there is no clear relationship between biases of models and soil sand content nor clay content. Therefore, the biases in these climate models are more closely related to soil moisture mean value than to soil properties. For SSM, ET, and P spectral slope ($SSM_{k\omega}$, $ET_{k\omega}$, and $P_{k\omega}$), models underestimate the memory of SSM, ET, and P for most regions, and this underestimation is most obvious in the lowest frequency range, i.e., at longer time scales (seasonal to annual). To summarize, our study identifies systematic metrics that can be used to assess model improvements of soil moisture variability.

Acknowledgments

The CMIP5 climate model data were available online (https://esgf-node.llnl.gov/). For the observation data of surface soil moisture, evapotranspiration, and precipitation, SMAP data can be obtained on https://earthdata.nasa.gov/, GLEAM data can be obtained on https://www.gleam.eu/, and ERA5 data can be obtained on https://cds.climate.copernicus.eu/. The GSDE soil data were also available online (http://globalchange.bnu.edu.cn/research/soilw). All codes related to this study can be found on https://github.com/xx2299/SSM. Gentine acknowledges funding from NASA 80NSSC18K0998.

References

Anber, U., Gentine, P., Wang, S., & Sobel, A. H. (2015). Fog and rain in the Amazon. *Proceedings of the National Academy of Sciences*, *112*(37), 11473-11477.

Akbar, R., Short Gianotti, D., McColl, K. A., Haghighi, E., Salvucci, G. D., & Entekhabi, D. (2018). Hydrological storage length scales represented by remote sensing estimates of soil moisture and precipitation. *Water Resources Research*, *54*(3), 1476-1492.

Berg, A., & Sheffield, J. (2018). Soil Moisture–Evapotranspiration Coupling in CMIP5 Models: Relationship with Simulated Climate and Projections. *Journal of Climate*, *31*(12), 4865-4878.

Botter, G., Peratoner, F., Porporato, A., Rodriguez-Iturbe, I., & Rinaldo, A. (2007). Signatures of large-scale soil moisture dynamics on streamflow statistics across US climate regimes. *Water resources research*, *43*(11).

Bourke, P. (1998). Generating noise with different power spectra laws. *accessed October*, *26*, 2006.

Brodzik, M. J., Billingsley, B., Haran, T., Raup, B., & Savoie, M. H. (2012). EASE-Grid 2.0: Incremental but significant improvements for Earth-gridded data sets. *ISPRS International Journal of Geo-Information*, *1*(1), 32-45.

Chan, S. K., Bindlish, R., O'Neill, P. E., Njoku, E., Jackson, T., Colliander, A., ... & Yueh, S. (2016). Assessment of the SMAP passive soil moisture product. *IEEE Transactions on Geoscience and Remote Sensing*, *54*(8), 4994-5007.

Chen, F., Crow, W. T., Bindlish, R., Colliander, A., Burgin, M. S., Asanuma, J., & Aida, K. (2018). Global-scale evaluation of SMAP, SMOS and ASCAT soil moisture products using triple collocation. *Remote Sensing of Environment*, *214*, 1-13.

Colliander, A., Jackson, T. J., Bindlish, R., Chan, S., Das, N., Kim, S. B., ... & Asanuma, J.

(2017). Validation of SMAP surface soil moisture products with core validation sites. *Remote Sensing of Environment*, *191*, 215-231.

Copernicus Climate Change Service (C3S) (2017): ERA5: Fifth generation of ECMWF atmospheric reanalyses of the global climate . Copernicus Climate Change Service Climate Data Store (CDS), *date of access*. https://cds.climate.copernicus.eu/cdsapp#!/home

Delworth, T. L., & Manabe, S. (1988). The influence of potential evaporation on the variabilities of simulated soil wetness and climate. *Journal of Climate*, *1*(5), 523-547.

D'odorico, P., Laio, F., Porporato, A., & Rodriguez-Iturbe, I. (2003). Hydrologic controls on soil carbon and nitrogen cycles. II. A case study. *Advances in Water Resources*, *26*(1), 59-70.

Entekhabi, D., Njoku, E. G., O'Neill, P. E., Kellogg, K. H., Crow, W. T., Edelstein, W. N., ... & Kimball, J. (2010). The soil moisture active passive (SMAP) mission. *Proceedings of the IEEE*, *98*(5), 704-716.

Flexas, M. M., Thompson, A. F., Torres, H. S., Klein, P., Farrar, J. T., Zhang, H., & Menemenlis, D. (2019). Global estimates of the energy transfer from the wind to the ocean, with emphasis on near-inertial oscillations. *Journal of Geophysical Research: Oceans*.

Ford, T. W., Harris, E., & Quiring, S. M. (2014). Estimating root zone soil moisture using near-surface observations from SMOS. *1foldr Import 2019-10-08 Batch 11*.

Ghannam, K., Nakai, T., Paschalis, A., Oishi, C. A., Kotani, A., Igarashi, Y., ... & Katul, G. G. (2016). Persistence and memory timescales in root-zone soil moisture dynamics. *Water Resources Research*, *52*(2), 1427-1445.

Green, J. K., Seneviratne, S. I., Berg, A. M., Findell, K. L., Hagemann, S., Lawrence, D. M., & Gentine, P. (2019). Large influence of soil moisture on long-term terrestrial carbon uptake. *Nature*, *565*(7740), 476.

Greve, P., Orlowsky, B., Mueller, B., Sheffield, J., Reichstein, M., & Seneviratne, S. I. (2014). Global assessment of trends in wetting and drying over land. *Nature geoscience*, *7*(10), 716.

Guillod, B. P., Orlowsky, B., Miralles, D. G., Teuling, A. J., & Seneviratne, S. I. (2015). Reconciling spatial and temporal soil moisture effects on afternoon rainfall. *Nature communications*, *6*, 6443.

Hsu, H., Lo, M. H., Guillod, B. P., Miralles, D. G., & Kumar, S. (2017). Relation between precipitation location and antecedent/subsequent soil moisture spatial patterns. *Journal of Geophysical Research: Atmospheres*, *122*(12), 6319-6328.

Jasechko, S., Sharp, Z. D., Gibson, J. J., Birks, S. J., Yi, Y., & Fawcett, P. J. (2013). Terrestrial water fluxes dominated by transpiration. *Nature*, *496*(7445), 347.

Katul, G. G., Porporato, A., Daly, E., Oishi, A. C., Kim, H. S., Stoy, P. C., ... & Siqueira, M. B. (2007). On the spectrum of soil moisture from hourly to interannual scales. *Water Resources Research*, *43*(5).

Kennedy, D., Swenson, S., Oleson, K. W., Lawrence, D. M., Fisher, R., Lola da Costa, A. C., & Gentine, P. (2019). Implementing plant hydraulics in the community land model, version 5. *Journal of Advances in Modeling Earth Systems*, *11*(2), 485-513.

Koster, R. D., Dirmeyer, P. A., Guo, Z., Bonan, G., Chan, E., Cox, P., ... & Liu, P. (2004). Regions of strong coupling between soil moisture and precipitation. *Science*, *305*(5687), 1138-1140.

Koster, R. D., & Suarez, M. J. (2001). Soil moisture memory in climate models. *Journal of hydrometeorology*, *2*(6), 558-570.

Martens, B., Miralles, D., Lievens, H., Fernández-Prieto, D., & Verhoest, N. E. (2016).

Improving terrestrial evaporation estimates over continental Australia through assimilation of SMOS soil moisture. *International Journal of Applied Earth Observation and Geoinformation*, *48*, 146-162.

Martens, B., Gonzalez Miralles, D., Lievens, H., Van Der Schalie, R., De Jeu, R. A., Fernández-Prieto, D., ... & Verhoest, N. (2017). GLEAM v3: Satellite-based land evaporation and root-zone soil moisture. *Geoscientific Model Development*, *10*(5), 1903-1925.

McColl, K. A., He, Q., Lu, H., & Entekhabi, D. (2019). Short-Term and Long-Term Surface Soil Moisture Memory Time Scales Are Spatially Anticorrelated at Global Scales. *Journal of Hydrometeorology*, *20*(6), 1165-1182.

Miralles, D. G., Holmes, T. R. H., De Jeu, R. A. M., Gash, J. H. C., Meesters, A. G. C. A., & Dolman, A. J. (2011a). Global land-surface evaporation estimated from satellite-based observations.

Miralles, D. G., De Jeu, R. A. M., Gash, J. H. C., Holmes, T. R. H., & Dolman, A. J. (2011b). Magnitude and variability of land evaporation and its components at the global scale.

O'Neill, P. E., S. Chan, E. G. Njoku, T. Jackson, and R. Bindlish. 2018. *SMAP L3 Radiometer Global Daily 36 km EASE-Grid Soil Moisture, Version 5*. Boulder, Colorado USA. NASA National Snow and Ice Data Center Distributed Active Archive Center. doi: https://doi.org/10.5067/ZX7YX2Y2LHEB.

Priestley, C. H. B., & Taylor, R. J. (1972). On the assessment of surface heat flux and evaporation using large-scale parameters. *Monthly weather review*, *100*(2), 81-92.

Salvucci, G. D., & Entekhabi, D. (1994). Equivalent steady soil moisture profile and the time compression approximation in water balance modeling. *Water Resources Research*, *30*(10), 2737-2749.

Seneviratne, S. I., Corti, T., Davin, E. L., Hirschi, M., Jaeger, E. B., Lehner, I., ... & Teuling, A. J. (2010). Investigating soil moisture–climate interactions in a changing climate: A review. *Earth-Science Reviews*, *99*(3-4), 125-161.

Seneviratne, S. I., & Koster, R. D. (2012). A revised framework for analyzing soil moisture memory in climate data: Derivation and interpretation. *Journal of Hydrometeorology*, *13*(1), 404-412.

Seneviratne, S. I., Koster, R. D., Guo, Z., Dirmeyer, P. A., Kowalczyk, E., Lawrence, D., ... & Verseghy, D. (2006). Soil moisture memory in AGCM simulations: analysis of global land–atmosphere coupling experiment (GLACE) data. *Journal of Hydrometeorology*, *7*(5), 1090-1112.

Shellito, P. J., Small, E. E., Colliander, A., Bindlish, R., Cosh, M. H., Berg, A. A., ... & Prueger, J. H. (2016). SMAP soil moisture drying more rapid than observed in situ following rainfall events. *Geophysical research letters*, *43*(15), 8068-8075.

Steele, J. H. (1985). A comparison of terrestrial and marine ecological systems. *Nature*, *313*(6001), 355.

Taylor, K. E., Stouffer, R. J., & Meehl, G. A. (2012). An overview of CMIP5 and the experiment design. *Bulletin of the American Meteorological Society*, *93*(4), 485-498.

Tuttle, S., & Salvucci, G. (2016). Empirical evidence of contrasting soil moisture–precipitation feedbacks across the United States. *Science*, *352*(6287), 825-828.

Vasseur, D. A., & Yodzis, P. (2004). The color of environmental noise. *Ecology*, *85*(4), 1146-1152.

Yang, X., Yong, B., Ren, L., Zhang, Y., & Long, D. (2017). Multi-scale validation of GLEAM evapotranspiration products over China via ChinaFLUX ET measurements. *International Journal of Remote Sensing*, *38*(20), 5688-5709.

Zhang, Y., Peña-Arancibia, J. L., McVicar, T. R., Chiew, F. H., Vaze, J., Liu, C., ... & Miralles, D. G. (2016). Multi-decadal trends in global terrestrial evapotranspiration and its components. *Scientific reports*, *6*, 19124.